

Direction-Dependent Polarised Primary Beams in Wide-Field Synthesis Imaging

D. A. Mitchell^{1,2}, R. B. Wayth³, G. Bernardi⁴, L. J. Greenhill⁴, and S. M. Ord³

¹*School of Physics, The University of Melbourne, Parkville, VIC 3010, Australia*

²*ARC Centre of Excellence for All-sky Astrophysics (CAASTRO)*

³*International Centre for Radio Astronomy Research, Curtin University, GPO Box U1987, Perth WA, 6845, Australia*

⁴*Harvard-Smithsonian Center for Astrophysics, 60 Garden St, Cambridge, MA 02138, USA*

Abstract

The process of wide-field synthesis imaging is explored, with the aim of understanding the implications of variable, polarised primary beams for forthcoming Epoch of Reionisation experiments. These experiments seek to detect weak signatures from redshifted 21cm emission in deep residual datasets, after suppression and subtraction of foreground emission. Many subtraction algorithms benefit from low side-lobes and polarisation leakage at the outset, and both of these are intimately linked to how the polarised primary beams are handled. Building on previous contributions from a number of authors, in which direction-dependent corrections are incorporated into visibility gridding kernels, we consider the special characteristics of arrays of fixed dipole antennas operating around 100-200 MHz, looking towards instruments such as the Square Kilometre Array (SKA) and the Hydrogen Epoch of Reionization Arrays (HERA). We show that integrating snapshots in the image domain can help to produce compact gridding kernels, and also reduce the need to make complicated polarised leakage corrections during gridding. We also investigate an alternative form for the gridding kernel that can suppress variations in the direction-dependent weighting of gridded visibilities by 10s of dB, while maintaining compact support.

1 Introduction

Synthesis imaging in radio astronomy is an indirect technique for measuring the radio sky brightness distribution. An array of radio receivers is used to measure the interference pattern of celestial radio waves, and the pattern is used to determine a sky brightness model. See, for example, Thompson et al. (2001). However, a number of simplifying assumptions that are commonly used in radio astronomy (such as small fields of view and identical antennas) are not valid for many new radio arrays. This is particularly true for new low-frequency arrays of fixed dipoles—for example, MWA (Lonsdale et al., 2009; Tingay et al., 2012), LOFAR (de Vos et al., 2009), PAPER (Parsons et al., 2010), and LWA (Ellingson et al., 2009; Taylor et al., 2012)—where advances in low-cost, high-performance electronics allow the deployment of many small phased-array antennas. Such antennas have a large field of view and can have complicated total power and polarisation responses on the sky. Most of these arrays will also search for the faint, diffuse signal coming from the Epoch of Reionisation (EoR, e.g., Furlanetto et al., 2006; Morales and Wyithe, 2010), for which foreground subtraction is a critical step (e.g., Morales et al., 2006). Recent observations have already reached the confusion level limit, well above the expected level required to detect the EoR signal (Bernardi et al., 2009, 2010; Williams et al., 2012; Bernardi et al., 2012). Very high fidelity imaging is required to accurately model the foreground sky, and this requirement motivates the present work. In the remainder of this section the problem will be laid out, and in subsequent sections the implications will be explored in more detail.

Over an infinitesimal range of observing time and frequency, an incident plane wave can be described by a 4-element column vector containing the self and cross coherence terms of the two electric field polarisations (Hamaker et al., 1996). The superposition of many such waves can be described by the spatial coherence of the electric field, and with enough samples this interference pattern can be inverted to reconstruct the incident power from the sky. However, when imaging across a wide field of view, angular response variations from sample to sample often limit the image quality that can be achieved by standard processing packages. There is significant effort underway to deal with the wide-field problem both in hardware, for instance the addition of a third axis of rotation to ASKAP antennas,¹ and in software, by applying direction-dependent corrections to each sample via convolution in the Fourier domain (e.g., Myers et al., 2003; Bhatnagar et al., 2008; Morales and Matejek, 2009; Smirnov, 2011).

Consider a radio interferometer that measures a complex, 4-element spatial-coherence column vector for each pair of spatially separated receivers (i.e., a vector containing the four polarised visibility measurements). The angular response of each receiver pair, or baseline, to each incident plane wave will in general be unique. It will be a function of receiver separation, the direction-dependent polarised primary beams of the two receivers, including the direction-dependent transform from sky polarisation coordinates to the polarised inputs of each receiver, and direction-dependent propagation effects. It is assumed that the signal paths remain linear, allowing the response of a given baseline to a given direction to be described by a 4×4 gain matrix multiplied by a geometric phase term.

For a given baseline, rather than thinking of a separate response matrix for each direction, instead consider a single 4×4 matrix with elements that are two-dimensional angular response functions. Multiplying this matrix with the angular distribution of radio emission, described as a 4×1 vector of two-dimensional brightness functions, results in a 4×1 vector containing the angular distribution of power seen by the baseline. The measured spatial-coherence vector can be modelled as the integral of these four functions over the field of view, or alternatively in the Fourier domain using convolutions. The Fourier domain representation is particularly useful for the reverse direction, going from visibilities to the sky, as it allows for a unique direction-dependent multiplication for each baseline.

In the following section the situation will be developed mathematically. In general, lower-case bold and italic symbols will refer to column vectors, while upper-case bold and italic symbols will refer to matrices. Variables that are functions of position in either the Fourier plane or image plane will be explicitly labeled.

2 Estimating Sky Brightness

Synthesis imaging involves the inversion of three-dimensional integrals, which are usually reduced to one or more two-dimensional segments or approximations, such as those described in Cornwell et al. (2003). These approaches can be computationally expensive and are complicated by variable polarisation coordinate systems, both between and within the two-dimensional segments. As an example, consider making images across the wide field-of-view of an array of dipole antennas that are fixed to the ground; even with ideal dipoles, polarised emission from radio sources at different positions on the curved sky will undergo different coordinate transformations, and these transformations will change with sidereal motion.

Before considering a more complicated brightness distribution, suppose that the sky is comprised of a single point source in direction $\boldsymbol{\sigma}'$, with a brightness described by polarised coherency vector, $\mathbf{b}(\boldsymbol{\sigma}')$, each element being a delta function centred at $\boldsymbol{\sigma}'$ (with units of $\text{W m}^{-2} \text{sr}^{-1} \text{Hz}^{-1}$). The k^{th} spatial-coherence sample reduces to

¹See the ASKAP Antenna Public Specification available at www.atnf.csiro.au/projects/askap/antennas.html.

$$\mathbf{r}_k = \mathbf{E}_k(\boldsymbol{\sigma}') \mathbf{b}(\boldsymbol{\sigma}') e^{-i2\pi \mathbf{u}_k \cdot \boldsymbol{\sigma}'} + \mathbf{n}_k, \quad (1)$$

where $\mathbf{E}_k(\boldsymbol{\sigma}')$ is a 4×4 matrix that describes the angular response of the sample to the sky, \mathbf{u}_k is the position vector of the sample's baseline measured in wavelengths, such that the exponent represents a geometric phase shift imposed by the baseline, and \mathbf{n}_k is a 4×1 column vector of independent measurement noise. From N such measurements, and assuming Gaussian-distributed measurement noise, a maximum-likelihood estimate of the incident coherency vector can be made using the normal equations (e.g., Press et al., 1986):

$$\hat{\mathbf{b}}(\boldsymbol{\sigma}') = \left(\sum_{k=1}^N \mathbf{E}_k(\boldsymbol{\sigma}')^\dagger \boldsymbol{\Lambda}_k \mathbf{E}_k(\boldsymbol{\sigma}') \right)^{-1} \left(\sum_{k=1}^N \mathbf{E}_k(\boldsymbol{\sigma}')^\dagger \boldsymbol{\Lambda}_k \mathbf{r}_k e^{i2\pi \mathbf{u}_k \cdot \boldsymbol{\sigma}'} \right) = \mathbf{D}(\boldsymbol{\sigma}')^{-1} \mathbf{d}(\boldsymbol{\sigma}'), \quad (2)$$

where the inverse-variance weight matrix, $\boldsymbol{\Lambda}_k$, is the inverse of the expectation of $\mathbf{n}_k \mathbf{n}_k^\dagger$, \mathbf{D} and \mathbf{d} represent the bracketed terms, and superscript \dagger denotes a conjugate transpose. See Ord et al. (2010) and Bernardi et al. (2012) for practical examples.

Consider now the more complicated case of simultaneously estimating the brightness in M directions, where the spatial-coherence vector for baseline k is

$$\mathbf{r}_k = \sum_{m=1}^M \mathbf{E}_k(\boldsymbol{\sigma}_m) \mathbf{b}(\boldsymbol{\sigma}_m) e^{-i2\pi \mathbf{u}_k \cdot \boldsymbol{\sigma}_m} + \mathbf{n}_k. \quad (3)$$

Equation (2) can be expanded for the $4M \times 1$ solution vector $[\hat{\mathbf{b}}(\boldsymbol{\sigma}_1), \hat{\mathbf{b}}(\boldsymbol{\sigma}_2), \dots, \hat{\mathbf{b}}(\boldsymbol{\sigma}_M)]^T$, where the right-hand bracketed term is replaced by $[\mathbf{d}(\boldsymbol{\sigma}_1), \mathbf{d}(\boldsymbol{\sigma}_2), \dots, \mathbf{d}(\boldsymbol{\sigma}_M)]^T$, a $4M \times 1$ vector of dirty measurements in the instrument frame, and the left-hand bracketed term is replaced by the inverse of the $4M \times 4M$ normal equation matrix, which contains the covariances of the incident coherency estimates.² The normal equation matrix will contain the 4×4 direction-dependent matrices defined in (2) along the diagonal, $\mathbf{D}(\boldsymbol{\sigma}_1), \mathbf{D}(\boldsymbol{\sigma}_2), \dots$, with polarised point spread function (PSF) side-lobes from other directions in off-diagonal elements. If the side-lobes of the array are small – or, for example, if they are being decreased in an iterative deconvolution process, as in Bhatnagar et al. (2008) – the matrix will be approximately block diagonal, allowing each direction to be approximately transformed to sky coordinates using (2). The remainder of this discussion will be limited to such local transformations, rather than full deconvolutions, and we will use the subscript d to indicate that a measurement, $\hat{\mathbf{b}}_d(\boldsymbol{\sigma}')$, is potentially corrupted by the side-lobes of other sources (i.e., is dirty).

For each sample, k , (3) has the form of a Fourier transform. It is common with imaging arrays to arrange the M directions of interest on a regular two-dimensional grid, as it is often computationally efficient to grid the samples onto the appropriate grid in Fourier space and use the Fast Fourier Transform (FFT) algorithm to calculate the M measurements, $\mathbf{d}(\boldsymbol{\sigma})$. When $\mathbf{E}_k(\boldsymbol{\sigma})$ is constant for all of the samples, the Fourier relationship holds for all k and the angular response of the samples can be dealt with after imaging. In addition, deconvolution is simplified because the PSF is shift-invariant. This is a common assumption in radio interferometry (Thompson et al., 2001). In general, however, the spatial-coherence samples will have different sky response matrices – for instance, due to different antenna responses or source motion across the sky. Any differences that affect the entire field of view in a consistent way (such as a time-dependent rotation of the parallactic angle for alt-az mounted dishes) can be dealt with using simple transformations prior to gridding, but for wide fields of view or when high dynamic range measurements are required, samples may require direction-dependent transformations to maintain the Fourier relationship.

²The $4M \times 4M$ matrix being inverted is typically large, ill-conditioned or singular, and limited by pixelisation effects. Iterative deconvolution methods can in general address all of these issues for radio sources with emission that is sufficiently strong.

When $\mathbf{E}_k(\boldsymbol{\sigma})$ does need to be accounted for on a sample-by-sample basis, direction-dependent multiplications can be applied during the FFT gridding step, as discussed in previous work (Bhatnagar et al., 2008; Rau et al., 2009; Morales and Matejek, 2009). Let $\mathbf{U}_k(\mathbf{u})$ be the matrix with elements that are the 2D Fourier transforms of the elements of $\mathbf{E}_k(\boldsymbol{\sigma})$, and consider polarisation product j of vector $\mathbf{d}(\boldsymbol{\sigma}')$. Writing the Fourier transform operations as integrals, to distinguish them from the gridding operations, and keeping in mind that the elements of r_k are samples, not functions of \mathbf{u} , we have

$$\begin{aligned}
 d_j(\boldsymbol{\sigma}') &= \sum_{k=1}^N \sum_{i=1}^4 \frac{1}{\sigma_{k,i}^2} E_{k,ij}^*(\boldsymbol{\sigma}') e^{i2\pi\mathbf{u}_k \cdot \boldsymbol{\sigma}'} r_{k,i} = \sum_{k=1}^N \sum_{i=1}^4 \frac{1}{\sigma_{k,i}^2} \iint_{-\infty}^{\infty} \{U_{k,ij}^*(\mathbf{u} - \mathbf{u}_k)\} e^{i2\pi\mathbf{u} \cdot \boldsymbol{\sigma}'} d\mathbf{u} r_{k,i} \\
 &= \iint_{-\infty}^{\infty} \left\{ \sum_{k=1}^N \sum_{i=1}^4 \frac{1}{\sigma_{k,i}^2} U_{k,ij}^*(\mathbf{u} - \mathbf{u}_k) r_{k,i} \right\} e^{i2\pi\mathbf{u} \cdot \boldsymbol{\sigma}'} d\mathbf{u}.
 \end{aligned} \tag{4}$$

This shows that, as desired, we can grid using kernels that are based on the FFT of the sample response functions, and form dirty images that are mathematically equivalent to the pixel-by-pixel direct Fourier transforms shown in (2).

Bhatnagar et al. (2008) consider applications where the $\mathbf{E}_k(\boldsymbol{\sigma})$ matrices are approximately unitary in every direction of interest (or, less stringently, where $\mathbf{E}_k(\boldsymbol{\sigma})^\dagger$ is approximately a scaled version of $\mathbf{E}_k(\boldsymbol{\sigma})^{-1}$). As they discuss, in a deconvolution scheme where one subtracts a sky model before gridding, high quality deconvolution comes from accurately estimating and subtracting the model visibilities. During the subsequent gridding and imaging step, the operations in (4) will produce nominally calibrated images in sky polarisation coordinates, due to the approximate unitarity of each $\mathbf{E}_k(\boldsymbol{\sigma})$. While not perfectly calibrated, these images will in many cases be good enough to incrementally update the sky model. However, the argument can be made more generally for any $\mathbf{E}_k(\boldsymbol{\sigma})$, as long as the appropriate $\mathbf{D}(\boldsymbol{\sigma})^{-1}$ is used to transform the dirty images back to sky coordinates before updating the sky model. In general there is not a one-to-one mapping between the sky, the visibilities, and the dirty images, and to use all of the available information all four spatial-coherency polarisations will need to be gridded into each of the four instrument polarisation images, as shown in (4).

For practical reasons it is typically assumed that, after standard direction-independent calibration, each $\mathbf{E}_k(\boldsymbol{\sigma})$ matrix has negligible off-diagonal elements, maintaining a one-to-one mapping between the sky and instrument coherence vectors. It is also typical to require that elements of $\mathbf{U}_k(\mathbf{u})$ have compact support (that is, are non-zero only for small \mathbf{u}), which is a reasonable assumption given the limited collecting area of antennas.³ These requirements are important, as the computational cost of gridding with large convolution kernels can be prohibitive. While much of this comes down to antenna design and engineering tolerances, small-scale structure in the celestial coordinates, particularly for large fields-of-view and fields near the celestial poles, will lead to large-scale features and off-diagonal terms in $\mathbf{U}_k(\mathbf{u})$.

If we instead grid to a coordinate system that is aligned with the receivers, such as one aligned with the ideal polarisation axes in a linearly polarised receiving system, much of the small-scale structure can be dealt with in the image plane. Furthermore, gridding in an antenna-based coordinate system should reduce the amount of information in the off-diagonal terms. Gridding in such a coordinate system is natural for arrays with antennas that track the sky, but this is not always feasible or desirable. It is also natural for snapshot imaging approaches that transform to the image plane regularly, as described later in this section.

If the angular response of sample k within an antenna-based frame is denoted $\mathbf{E}_{Ak}(\boldsymbol{\sigma})$, such that $\mathbf{E}_k(\boldsymbol{\sigma}) =$

³The 3D nature of some antennas will result in power being distributed across 2D Fourier space, but for the purposes of this paper we will assume the effect is negligible.

$\mathbf{E}_{Ak}(\boldsymbol{\sigma})\mathbf{C}(\boldsymbol{\sigma})$, and if the feed configuration matrix that transforms between frames, $\mathbf{C}(\boldsymbol{\sigma})$, is constant across the samples, then one can form an alternative dirty image

$$\mathbf{d}_A(\boldsymbol{\sigma}) = \sum_{k=1}^N \mathbf{E}_{Ak}(\boldsymbol{\sigma})^\dagger \boldsymbol{\Lambda}_k e^{i2\pi \mathbf{u}_k \cdot \boldsymbol{\sigma}} \mathbf{r}_k = \mathcal{F} \left\{ \sum_{k=1}^N \mathbf{U}_{Ak}(\mathbf{u} - \mathbf{u}_k)^\dagger \boldsymbol{\Lambda}_k \mathbf{r}_k \right\}, \quad (5)$$

where $\mathcal{F}\{\dots\}$ denotes the element-by-element Fourier transform described above for $\mathbf{U}(\mathbf{u})$ and $\mathbf{E}(\boldsymbol{\sigma})$. Substituting for $\mathbf{E}_k(\boldsymbol{\sigma})$ in (2) results in a single transformation to sky coordinates, applied in the image plane:

$$\hat{\mathbf{b}}_d(\boldsymbol{\sigma}) = \mathbf{C}(\boldsymbol{\sigma})^{-1} \left(\sum_{k=1}^N \mathbf{E}_{Ak}(\boldsymbol{\sigma})^\dagger \boldsymbol{\Lambda}_k \mathbf{E}_{Ak}(\boldsymbol{\sigma}) \right)^{-1} \mathbf{d}_A(\boldsymbol{\sigma}), \quad (6)$$

where the subscript d indicates that the estimate is dirty, in that while each pixel has been transformed to sky coordinates and de-weighted, the pixel coupling contained in the $4M \times 4M$ normal equation matrix has not been dealt with. Figure 1 gives examples of these functions for MWA-style antennas with various calibration errors.

When tracking a patch of sky with some types of steerable antennas, matrix $\mathbf{C}(\boldsymbol{\sigma})$ will not change with time, except for a possible parallactic rotation that is the same for each $\boldsymbol{\sigma}$ and therefore straightforward to account for in the Fourier domain. The situation is quite different for an array of dipole antennas that are fixed to the ground. The structure in $\mathbf{C}(\boldsymbol{\sigma})$ will change with time in a direction-dependent fashion, becoming more pronounced as the field size increases. These changes will need to be incorporated into the $\mathbf{U}_{Ak}(\mathbf{u})$ matrices, potentially increasing the size of the gridding kernels and the relevance of the off-diagonal terms. The longer one integrates, the more the matrices $\mathbf{C}(\boldsymbol{\sigma})$ will change, and in general there will be a trade-off between the time interval over which one can integrate visibility samples and the compactness of $\mathbf{U}_{Ak}(\mathbf{u})$. This situation is alleviated in snapshot imaging, where much of the structure can be dealt with from snapshot to snapshot in the image plane, using a time-dependent matrix, $\mathbf{C}_t(\boldsymbol{\sigma})$. In this case (2) and (5) can be combined to give

$$\hat{\mathbf{b}}_d(\boldsymbol{\sigma}) = \left(\sum_{t=1}^T \sum_{k=1}^N \mathbf{E}_{kt}(\boldsymbol{\sigma})^\dagger \boldsymbol{\Lambda}_{kt} \mathbf{E}_{kt}(\boldsymbol{\sigma}) \right)^{-1} \sum_{t=1}^T \mathbf{C}_t(\boldsymbol{\sigma})^\dagger \mathcal{F} \left\{ \sum_{k=1}^N \mathbf{U}_{Akt}(\mathbf{u} - \mathbf{u}_k)^\dagger \boldsymbol{\Lambda}_{kt} \mathbf{r}_{kt} \right\}. \quad (7)$$

Snapshot imaging has been avoided in the past due to computational concerns and the desire to enhance deconvolution by maintaining a constant PSF during an observation (e.g., Cornwell and Perley, 1992; Perley, 1999). However, it should be clear from equation 2 and onwards that in general the convolution theorem will not hold, and the PSF will vary with both direction and time, regardless of the wide-field imaging strategy. Snapshot imaging software has been developed to image data from arrays such as the MWA and the Large Aperture Experiment to Detect the Dark Ages (LEDA, see Greenhill and Bernardi, 2012), enabling image-based corrections for most of the polarisation structure, for wide-field w-terms, and for direction-dependent position shifts and Faraday rotation caused by the ionosphere (see, for example, Mitchell et al., 2008; Ord et al., 2010; Tingay et al., 2012). These arrays are also being designed to have dense sampling in \mathbf{u} , giving more control of the PSF and helping to minimise the drawbacks of joint deconvolution.⁴ Developments are also being made on image-domain deconvolution approaches, which allow for direction- and time-dependent PSFs (Pindor et al., 2011; Bernardi et al., 2011; Williams et al., 2012; Sullivan et al., 2012).

⁴Since the convolution theorem does not in general hold, the term deconvolution is a misnomer. However, as it is used more generally in radio astronomy we will stick with the jargon in this paper.

Before moving on to discuss these concepts further, a few of them should be reiterated. Any direction-dependent structure in the angular response matrices that is constant for all samples can be dealt with once, after imaging. Similarly, components of the matrices that are constant across the image can be dealt with before visibility gridding. However, direction-dependent structure that differs from sample to sample may require direction-dependent modifications during gridding, using Fourier transforms of the angular response functions. Gridding is computationally expensive, so it is desirable for the angular response functions to have compact support in Fourier space, to minimise the gridding kernel size. Furthermore, while in many situations the polarised angular response matrices can be assumed to be diagonal, resulting in a one-to-one mapping between the sky, the visibilities, and the dirty images, in general this is not the case. Any non-negligible off-diagonal terms result in extra gridding, so it is desirable to suppress them where possible. Dipole arrays are precisely the type with substantial off-diagonal elements. The wide-field arrays coming on-line this decade will provide important for understanding how susceptible various array designs are to these problems.

Gridding in an antenna-based coordinate system, rather than a sky-based system, can help to both reduce the off-diagonal terms of the polarised angular response matrices and keep the gridding kernels compact. However, for arrays of dipoles that are fixed to the ground, the sky coordinates will rotate in a direction-dependent fashion within an antenna-based system, and there will be a trade-off between integration time in Fourier space and both kernel size and off-diagonal amplitudes. Snapshot imaging approaches—which are being developed for arrays of many small antennas, to deal with ionospheric distortions, wide-field effects, and ever higher bit rates from correlators—transform samples to the image plane regularly, allowing much of the time-dependent variability to be accounted for in the image plane and keeping the kernels compact.

Some of these concepts are shown graphically in section 4, along with the concepts that are discussed below.

3 Alternative Gridding Kernels

In radio astronomy it is common to weight and taper the visibility samples being gridded, to control properties of the PSF and image noise. Two standard weighting types are natural weighting, where each sample is given the same weight (or in some schemes weights proportional to the inverse of the sample noise variance), and uniform weighting, where the local density of samples is divided out (or the local density of weights, if visibilities are inverse-variance weighted), giving different regions of Fourier space equal weight. Under the common assumptions of traditional synthesis imaging, natural weighting gives the lowest image noise, while uniform weighting reduces PSF side-lobes, since in effect it is normalising the Fourier coefficients. Schemes such as robust weighting try to get the best of both worlds, for instance by uniform weighting and then applying a smooth taper that roughly follows the gross distribution of samples (i.e., retaining much of the low-noise weighting but removing small-scale weight variations that will ring in image space).

The direction-dependent gridding described in the previous section is effectively an extension of natural weighting, taken to the extreme of accounting for gain differences of different samples in different directions. As in natural weighting, the aim is to minimise thermal noise in the image, given adequate deconvolution. While one can attempt to apply robust weighting to lower the side-lobes, it is also worth asking whether alternative gridding kernels can be used as a direction-dependent extension to uniform weighting, as one might expect that normalising the Fourier coefficients in a direction and sample dependent fashion might help to suppress structure (or structure variation) in the PSF.

Naively, one might hope to use the inverse of the sample response matrix, $\mathcal{F}\{\mathbf{E}_k(\boldsymbol{\sigma})^{-1}\}$. This has a major drawback: discontinuities in the polarised response, such as nulls, will become sharp features that will ring out across Fourier space and result in large, complicated gridding kernels. The noise properties of the gridded visibilities will also be undesirable. An alternative gridding function that shows some promise for situations

where the $\mathbf{E}_k(\boldsymbol{\sigma})$ matrices can be considered diagonal (so that any primary beam discontinuities are likely to be approximately aligned, which is not the case for cross-polarisations) is

$$K_{k,ii}(\mathbf{u}) = \mathcal{F} \left\{ \bar{E}_{ii}^*(\boldsymbol{\sigma}) \bar{E}_{ii}(\boldsymbol{\sigma}) (E_{k,ii}(\boldsymbol{\sigma}) + \epsilon)^{-1} \right\}, \quad (8)$$

where subscript ii indicates diagonal element i , the overbar indicates an average or ideal model, and ϵ is used to limit the depth of nulls in the denominator. While the kernels discussed in section 2 result in gridded visibilities that are weighted by the square of the angular response, this type of kernel aims to replace sample-to-sample variations and weight by the square of the average angular response. This has various benefits:

- Deep nulls in $\bar{E}_{ii}^*(\boldsymbol{\sigma}) \bar{E}_{ii}(\boldsymbol{\sigma})$ will typically suppress areas where there are nulls in $E_{k,ii}(\boldsymbol{\sigma})$, and will therefore also suppress ringing in the kernels.
- If discontinuities arising from the inverse in (8) are avoided, the gridding kernel should have comparable compact support to that of $\mathcal{F} \{ \bar{E}_{ii}^*(\boldsymbol{\sigma}) \}$. This is shown for simulated array elements comprising a 4×4 grid of dipoles in figure 4.
- The gridded samples retain the average direction-dependent weighting, which will often be more significant than sample-to-sample variations.
- Except for a possible pixel-by-pixel transformation from an antenna-based reference frame to the sky frame, the resulting images are correctly weighted for integration in the image domain, for instance when integrating snapshots or performing image-domain mosaicing.
- $\bar{E}_{ii}^*(\boldsymbol{\sigma}) \bar{E}_{ii}(\boldsymbol{\sigma})$ is constant across all of the samples, which should in general reduce structure and direction dependence in the PSF. It can also simplify weighting: the natural and uniform weighting schemes discussed above are usually based on the assumption that the samples have equal gain, but the kernels discussed in section 2 result in gridded samples that have direction-dependent gain, and the normalisation for one direction may not be right for other directions.
- Over a short enough bandwidth, one could choose $\bar{E}_{ii}^*(\boldsymbol{\sigma}) \bar{E}_{ii}(\boldsymbol{\sigma})$ to be independent of frequency, in an attempt to remove frequency-dependent structure from the PSF. While this would not result in the optimal weighting required to minimise thermal noise after image integration, it may prove beneficial for some of the foreground-subtraction procedures being researched for 21cm power spectrum experiments (such as those described in Bowman et al., 2009).

The details of how these alternative kernels compare with those of section 2 depend on issues such as the type of antenna, the level of primary beam variation, the density of samples, and the type of weighting applied before the FFT. The authors are investigating whether both kernel types might have a place in an iterative deconvolution and imaging scheme; for instance, using the kernels from section 2 while optimising the sky models, to make the most of signal-to-noise ratios, and using the alternative kernels discussed above in the final iteration to reduce the side-lobes and position-dependence of the PSF in the residual images used for EoR observations. This work will be the basis of a follow-up paper.

4 Examples

Consider a simulated array of crossed dipoles on ground screens, which have the zenith at boresight and dipoles aligned with North and East in the horizontal coordinate system. Furthermore, suppose the array is at latitude L and that the dipoles are grouped into MWA-style antenna tiles comprising 16 dipoles. Figures 1 through 4 show functions from various elements of the $\mathbf{E}_k(\boldsymbol{\sigma})$, $\mathbf{U}_k(\boldsymbol{\sigma})$ and $\mathbf{C}(\boldsymbol{\sigma})$ matrices for these antenna tiles. Tile

primary beams are modelled as the superposition of the 16 dipole gain patterns, described below, and they are distorted by the addition of direction-independent Gaussian noise to the gain and phase of each dipole with an RMS of 10% and 5° respectively. The dipoles were separated by 1.1 m at a height of 0.3 m above a ground plane, with Gaussian-distributed position errors of 0.01 m RMS in each direction, and Gaussian-distributed rotation errors of 1° RMS in azimuth. Gaussian-distributed errors in the boresight of each tile were also added, with an RMS of 1° from zenith in both directions. While these errors are somewhat realistic, they should not be thought of as representative for MWA, as they were chosen rather arbitrarily. In direction $\boldsymbol{\sigma}$, the feed configuration matrix, $\mathbf{C}(\boldsymbol{\sigma})$, has been constructed from the tensor product of the 2×2 dipole feed configuration Jones matrix, $\mathbf{c}(\boldsymbol{\sigma})$, with itself, where $\mathbf{c}(\boldsymbol{\sigma})$ converts from the standard equatorial coordinates of the celestial sphere to the local North and East coordinates:

$$\mathbf{c}(\boldsymbol{\sigma}) = \begin{bmatrix} \cos L \cos \delta(\boldsymbol{\sigma}) + \sin L \sin \delta(\boldsymbol{\sigma}) \cos H(\boldsymbol{\sigma}), & -\sin L \sin H(\boldsymbol{\sigma}) \\ \sin \delta \sin H(\boldsymbol{\sigma}), & \cos H(\boldsymbol{\sigma}) \end{bmatrix}, \quad (9)$$

where $H(\boldsymbol{\sigma})$ and $\delta(\boldsymbol{\sigma})$ are the hour angle and declination of direction $\boldsymbol{\sigma}$ respectively.

Figure 1 shows elements of $\mathbf{E}_k(\boldsymbol{\sigma})$, $\mathbf{U}_k(\mathbf{u})$, $\mathbf{C}(\boldsymbol{\sigma})$, and $\mathbf{U}_{Ak}(\mathbf{u})$, averaged over k . The simulation is for the extreme case of imaging the entire sky with antenna primary beams that are pointed close to the south celestial pole, as can be seen from the four angular response patterns in the top row. The second row down shows the effect of describing all of the polarised response information in Fourier space: the off-diagonal terms have large amplitudes, and much of the information is distributed across Fourier space. The bottom row shows similar Fourier domain functions, except that the complicated feed configuration functions (shown in the middle row) were removed, to be dealt with in the image domain. In this antenna-based coordinate system, all of the elements are seen to have compact support and much reduced off-diagonal amplitudes.

Figures 2 and 3 show elements of $\mathbf{E}_k(\boldsymbol{\sigma})$, $\mathbf{U}_k(\mathbf{u})$, and $\mathbf{U}_{Ak}(\mathbf{u})$, when imaging smaller fields. The panels show the effect of sidereal motion on the angular response functions of a single sample. In each figure, the second row shows that, once again, describing all of the polarised response information in Fourier space leads to off-diagonal terms with large amplitudes. In the third row of each figure, the feed configuration matrix for the centre of the image has been used in an attempt to align each snapshot in a direction-independent fashion, much like parallactic-angle corrections for alt-az parabolic dish antennas. The off-diagonal terms are reduced in amplitude—more so for the smaller field, as one might expect—however not as much as after full conversion to the antenna-based system, as shown in the bottom row of each figure.

Figure 4 gives a comparison of the two gridding approaches discussed in sections 2 and 3. It can be seen that, for this type of primary beam function, both approaches produce kernels with similar support in Fourier space, and the alternative kernel type discussed in section 3 can produce gridded response patterns with reduced variation from sample to sample.

5 Summary

Direction-dependent gridding is reviewed from the perspective of low frequency dipole arrays. It is seen that the approach discussed by Bhatnagar et al. (2008) is quite general and can be applied to arrays of dipoles, however temporal and angular variations in the feed configuration relative to the sky mean that the gridding kernel extent will likely increase the longer one averages samples in Fourier space.

It is seen that snapshot imaging followed by image-based weighting and averaging can help to keep the amount of computation involved in visibility gridding to a minimum. Since, at any instant, many current and planned arrays have baselines that lie close to a two-dimensional plane, the simplifications offered by snapshot imaging

couple well with the warped-snapshot wide-field imaging technique discussed in Bracewell (1984); Cornwell and Perley (1992); Perley (1999); Cornwell et al. (2003); and Ord et al. (2010).

While the maximum-likelihood approach reviewed in section 2 is in many respects ideal for making sky images, it is aimed at structure that is above the image noise. Any sky structure that is at the noise level – or the noise itself for images that are limited by confusion – retains the PSF, which in general will be position, polarisation, time and frequency dependent. This could limit the extraction of science signals that are buried in the noise, such as the angular power spectrum of redshifted 21cm emission from neutral Hydrogen. We introduced an alternative gridding scheme in section 3, with the aim of reducing side-lobe structure by reducing Fourier coefficient structure that is due to the array.

Acknowledgements

Support came from the U.S. National Science Foundation (grants AST-0457585 and PHY-0835713). The Centre for All-sky Astrophysics is an Australian Research Council Centre of Excellence, funded by grant CE11E0090. The International Centre for Radio Astronomy Research is a Joint Venture between Curtin University and The University of Western Australia, funded by the State Government of Western Australia and the Joint Venture partners. R.B.W is supported via the Western Australian Centre of Excellence in Radio Astronomy Science and Engineering.

References

- Bernardi, G., Mitchell, D. A., Ord, S. M., Greenhill, L. J., Pindor, B., Wayth, R. B., and Wyithe, J. S. B. (2011). Subtraction of point sources from interferometric radio images through an algebraic forward modeling scheme. *MNRAS*, 413(1):411–422.
- Bernardi et al., G. (2009). Foregrounds for observations of the cosmological 21 cm line. I. First Westerbork measurements of Galactic emission at 150 MHz in a low latitude field. *A&A*, 500(3):965–979.
- Bernardi et al., G. (2010). Foregrounds for observations of the cosmological 21 cm line. II. Westerbork observations of the fields around 3C 196 and the North Celestial Pole. *A&A*, 522:67.
- Bernardi et al., G. (2012). A 2400 Square Degree Survey at 200 MHz: Bright Sources, Foregrounds and Polarization. In prep.
- Bhatnagar, S., Cornwell, T. J., Golap, K., and Uson, J. M. (2008). Correcting direction-dependent gains in the deconvolution of radio interferometric images. *A&A*, 487(1):419–429.
- Bowman, J. D., Morales, M. F., and Hewitt, J. N. (2009). Foreground Contamination in Interferometric Measurements of the Redshifted 21 cm Power Spectrum. *ApJ*, 695:183.
- Bracewell, R. N. (1984). Inversion of nonplanar visibilities. In Roberts, J. A., editor, *Indirect Imaging*, volume 177. Cambridge: Cambridge University Press.
- Cornwell, T. J., Golap, K., and Bhatnagar, S. (2003). W Projection: A New Algorithm for Non-Coplanar Baselines. *EVLA Memo*, 67.
- Cornwell, T. J. and Perley, R. A. (1992). Radio-interferometric imaging of very large fields - The problem of non-coplanar arrays. *A&A*, 261:353–364.

- de Vos, M., Gunst, A. W., and Nijboer, R. (2009). The LOFAR Telescope: System Architecture and Signal Processing. *Proc. IEEE*, 97(9):1431–1437.
- Ellingson, S. W., Clarke, T. E., Cohen, A., Craig, J., Kassim, N. E., Pihlstrom, Y., Rickard, L. J., and Taylor, G. B. (2009). The Long Wavelength Array. *Proc. IEEE*, 97(8):1421–1430.
- Furlanetto, S. R., Oh, S. P., and Briggs, F. (2006). Cosmology at Low Frequencies: The 21 cm Transition and the High-Redshift Universe. *Physics Reports*, 433:181.
- Greenhill, L. J. and Bernardi, G. (2012). HI Epoch of Reionization Arrays. In Komonjinda, S., Kovalev, Y., and Ruffolo, D., editors, *11th Asian-Pacific Regional IAU Meeting 2011*, volume 1 of *NARIT Conference Series*. Bangkok, NARIT.
- Hamaker, J. P., Bregman, J. D., and Sault, R. J. (1996). Understanding radio polarimetry. I. Mathematical foundations. *A&A Suppl. Ser.*, 117:137–147.
- Lonsdale et al., C. J. (2009). The murchison widefield array: Design overview. *Proc. IEEE*, 97(8):1497–1506.
- Mitchell, D. A., Greenhill, L. J., Wayth, R. B., Sault, R. J., Lonsdale, C. J., Cappallo, R. J., Morales, M. F., and Ord, S. M. (2008). Real-time calibration of the murchison widefield array. *IEEE Journal of Selected Topics in Signal Processing*, 2:1993–2006.
- Morales, M. F., Bowman, J. D., and Hewitt, J. N. (2006). Improving Foreground Subtraction in Statistical Observations of 21 cm Emission from the Epoch of Reionization. *ApJ*, 648:767.
- Morales, M. F. and Matejek, M. (2009). Software holography: interferometric data analysis for the challenges of next generation observatories. *MNRAS*, 400(4):1814–1820.
- Morales, M. F. and Wyithe, J. S. B. (2010). Reionization and Cosmology with 21-cm Fluctuations. *Annual Review of Astronomy and Astrophysics*, 48:127–171.
- Myers, S. T., Contaldi, C. R., R. Bond, J., Pen, U.-L., Pogosyan, D., Prunet, S., Sievers, J. L., Mason, B. S., Pearson, T. J., Readhead, A. C. S., and Shepherd, M. C. (2003). A Fast Gridded Method for the Estimation of the Power Spectrum of the Cosmic Microwave Background from Interferometer Data with Application to the Cosmic Background Imager. *ApJ*, 591(2):575–598.
- Ord et al., S. (2010). Interferometric imaging with the 32 element murchison wide-field array. *PASP*.
- Parsons, A. R., Backer, D. C., Foster, G. S., Wright, M. C. H., Bradley, R. F., Gugliucci, N. E., Parashare, C. R., Benoit, E. E., Aguirre, J. E., Jacobs, D. C., Carilli, C. L., Herne, D., Lynch, M. J., Manley, J. R., and Werthimer, D. J. (2010). The Precision Array for Probing the Epoch of Reionization: 8 Station Results. *AJ*, 139(4):1468–1480.
- Perley, R. A. (1999). Lecture 19. Imaging with Non-Coplanar Arrays. In Taylor, G. B., Carilli, C. L., and Perley, R. A., editors, *Synthesis Imaging in Radio Astronomy II*, volume 180 of *Astronomical Society of the Pacific Conference Series*, pages 383–400. Astronomical Society of the Pacific.
- Pindor, B., Wyithe, J. S. B., Mitchell, D. A., Ord, S. M., Wayth, R. B., and Greenhill, L. J. (2011). Subtraction of Bright Point Sources from Synthesis Images of the Epoch of Reionization. *PASA*, 28(1):46–57.
- Press, W. H., Flannery, B. P., Teukolsky, S. A., and Vetterling, W. T. (1986). *Numerical Recipes: The Art of Scientific Computing*. Cambridge University Press, first edition.
- Rau, U., Bhatnagar, S., Voronkov, M. A., and Cornwell, T. J. (2009). Advances in Calibration and Imaging Techniques in Radio Interferometry. *Proc. IEEE*, 97(8):1472–1481.

- Smirnov, O. M. (2011). Revisiting the radio interferometer measurement equation. ii. calibration and direction-dependent effects. *A&A*, 527.
- Sullivan et al., I. S. (2012). Fast Holographic Deconvolution: A New Technique for Precision Radio Interferometry. In prep.
- Taylor et al., G. B. (2012). First Light for the First Station of the Long Wavelength Array. In prep.
- Thompson, A. R., Moran, J. M., and Jr, G. W. S. (2001). *Interferometry and Synthesis in Radio Astronomy, 2nd Edition*. New York: Wiley-Interscience.
- Tingay et al., S. J. (2012). The Murchison Widefield Array: A Square Kilometre Array Precursor at low radio frequencies. In prep.
- Williams et al., C. L. (2012). Low Frequency Imaging of Fields at High Galactic Latitude with the Murchison Widefield Array 32-Element Prototype. Submitted to ApJ.

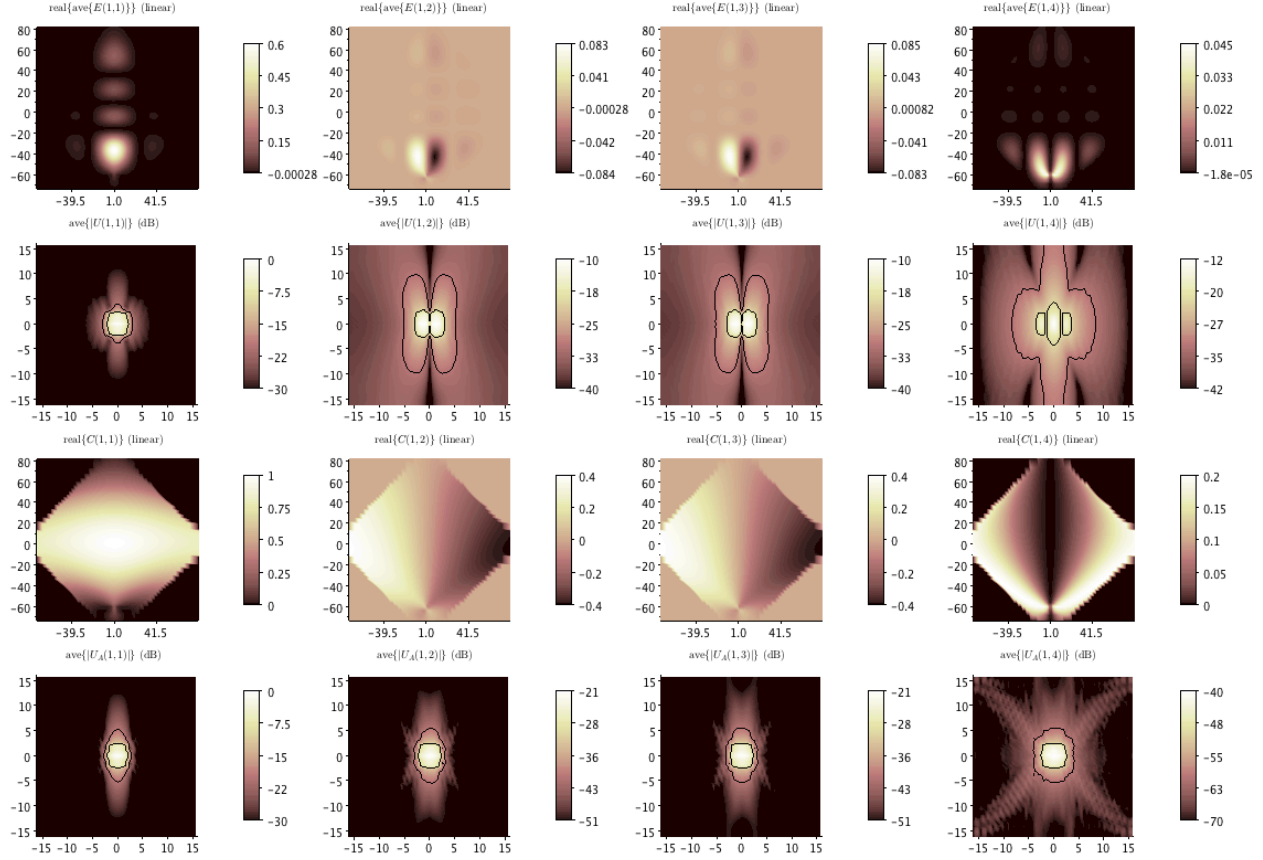


Figure 1: The panels show all-sky angular response functions and their FFTs for MWA-style antenna tiles, averaged over 50 samples in a single snapshot. They demonstrate how moving to an antenna-based coordinate system reduces the amplitude and extent of the off-diagonal FFT terms, as described in section 2. Reading down each column, we have elements of $\mathbf{E}_k(\boldsymbol{\sigma})$, $\mathbf{U}_k(\mathbf{u})$, $\mathbf{C}(\boldsymbol{\sigma})$, and $\mathbf{U}_{Ak}(\mathbf{u})$. Each column represents one of the 16 matrix elements, these four being those associated with the first element of each spatial-coherency sample. In the image domain, the real components are shown, with linear amplitude scaling and $\boldsymbol{\sigma}$ in degrees. The structure towards the bottom of the images is due to the south celestial pole. In the Fourier domain, averages are over the absolute values, functions have logarithmic amplitude scaling (running from -30 dB to 0 dB relative to the panel maximum, all scaled to the maximum of element 1,1), and \mathbf{u} is in wavelengths. Tile primary beams are modelled as the superposition of 16 dipole angular response matrices with various dipole-based errors, as described in the main text, and these imperfections set the final level of leakage that is achieved in an antenna-based coordinate system, shown in the bottom row of panels. The high level of leakage seen for the sky-based coordinate system, shown in the second row, which is as much as 10% of the amplitude in the 1,1 diagonal element and extends across Fourier space, is due to the structure in $\mathbf{C}(\boldsymbol{\sigma})$, and highlights the benefit of gridding in an antenna-based coordinate system.

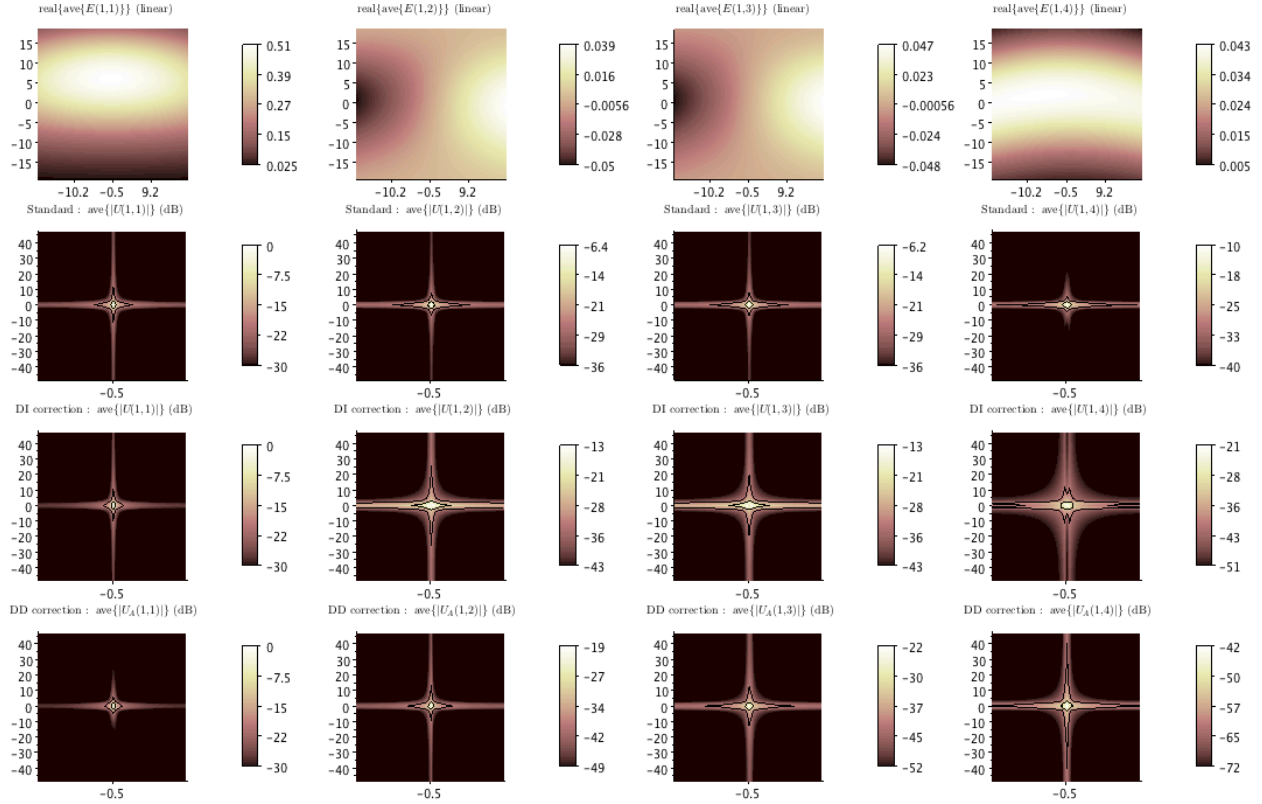


Figure 2: The panels show $\sim 40^\circ \times 40^\circ$ angular response functions and their FFTs for MWA-style antenna tiles, averaged over 7 snapshots for a single baseline (hour angle = $[-3,3]$, declination $\sim -71^\circ$). They demonstrate once again the benefit of moving to an antenna-based coordinate system, as described in section 2. Reading down each column, we have elements of $\mathbf{E}_k(\boldsymbol{\sigma})$, $\mathbf{U}_k(\mathbf{u})$, $\mathbf{U}'_k(\mathbf{u})$, and $\mathbf{U}_{Ak}(\mathbf{u})$. In the image domain, the real components are shown, with linear amplitude scaling and $\boldsymbol{\sigma}$ in degrees. In the Fourier domain, averages are over the absolute values, functions have logarithmic amplitude scaling (running from -30 dB to 0 dB relative to the panel maximum, all scaled to the maximum of element 1,1), and \mathbf{u} is in wavelengths. Tile primary beams are modelled as the superposition of 16 dipole angular response matrices with various dipole-based errors, as described in the main text, and these imperfections set the final level of leakage that is achieved in an antenna-based coordinate system, shown in the bottom row of panels. The high level of leakage seen for the sky-based coordinate system, shown in the second row, is due to the structure in $\mathbf{C}(\boldsymbol{\sigma})$. The second to last row shows averaged kernels for the situation where the 4×4 feed configuration matrix at the centre of each snapshot, $\mathbf{C}(\boldsymbol{\sigma}_0)$, is applied to the spatial-coherency sample directly, before gridding. This direction-independent (DI) correction allows the removal of $\mathbf{C}(\boldsymbol{\sigma}_0)$ from the kernels, leading to the reduction that is seen in the off-diagonal amplitudes. This is akin to a parallactic angle rotation for alt-az dishes, however here the correction is only exact at the centre of the image. While not as good as the full direction-dependent (DD) conversion to an antenna-based system, it does reduce the leakage seen in the second row.

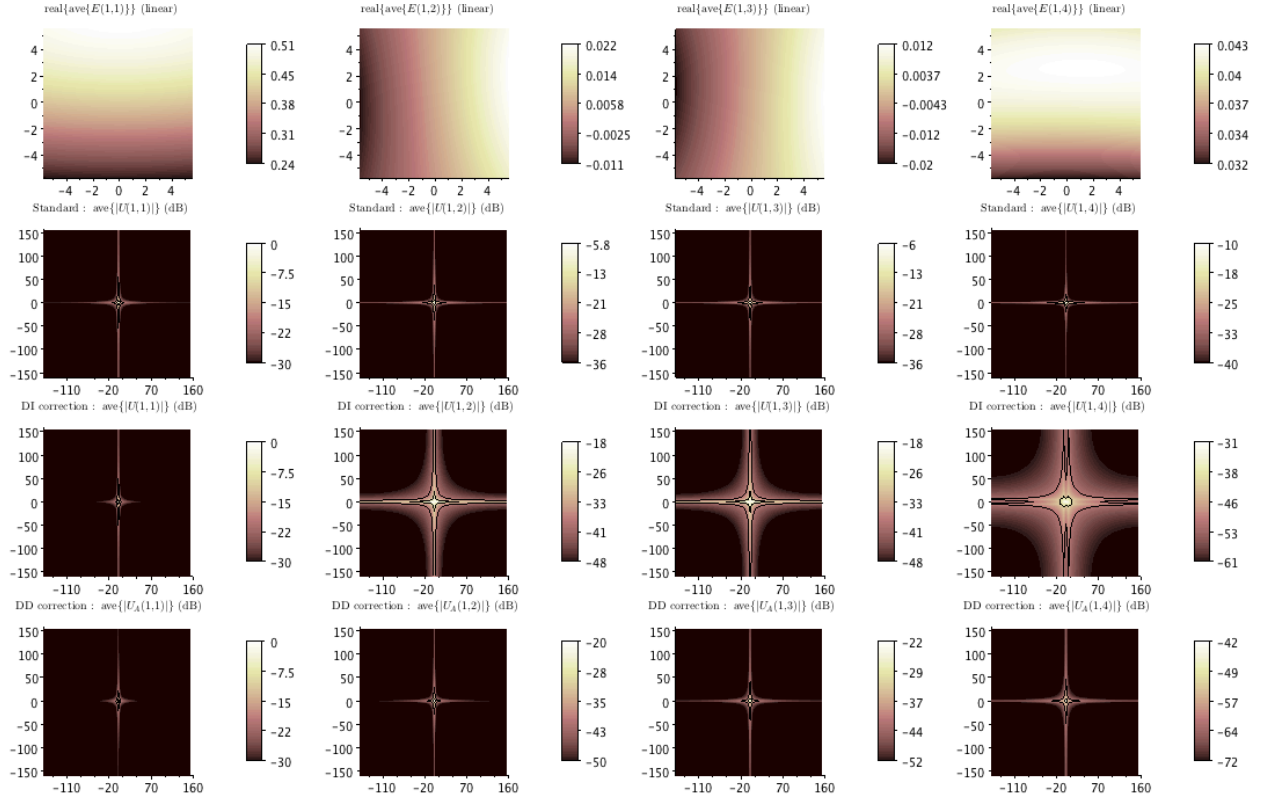


Figure 3: The same as figure 2, however here the image size has been reduced to $\sim 12^\circ \times 12^\circ$. As in the previous figure, the second to last row shows averaged kernels for the situation where the 4×4 feed configuration matrix at the centre of each snapshot, $C(\sigma_0)$, is applied to the spatial-coherency sample directly, before gridding. This direction-independent (DI) correction allows the removal of $C(\sigma_0)$ from the kernels. The correction is only exact at the centre of the image, and as expected for a reduced field size, the amplitudes of the off-diagonal terms are closer to those of the full direction-dependent (DD) conversion to an antenna-based system, compared with those of the larger field shown in figure 2.

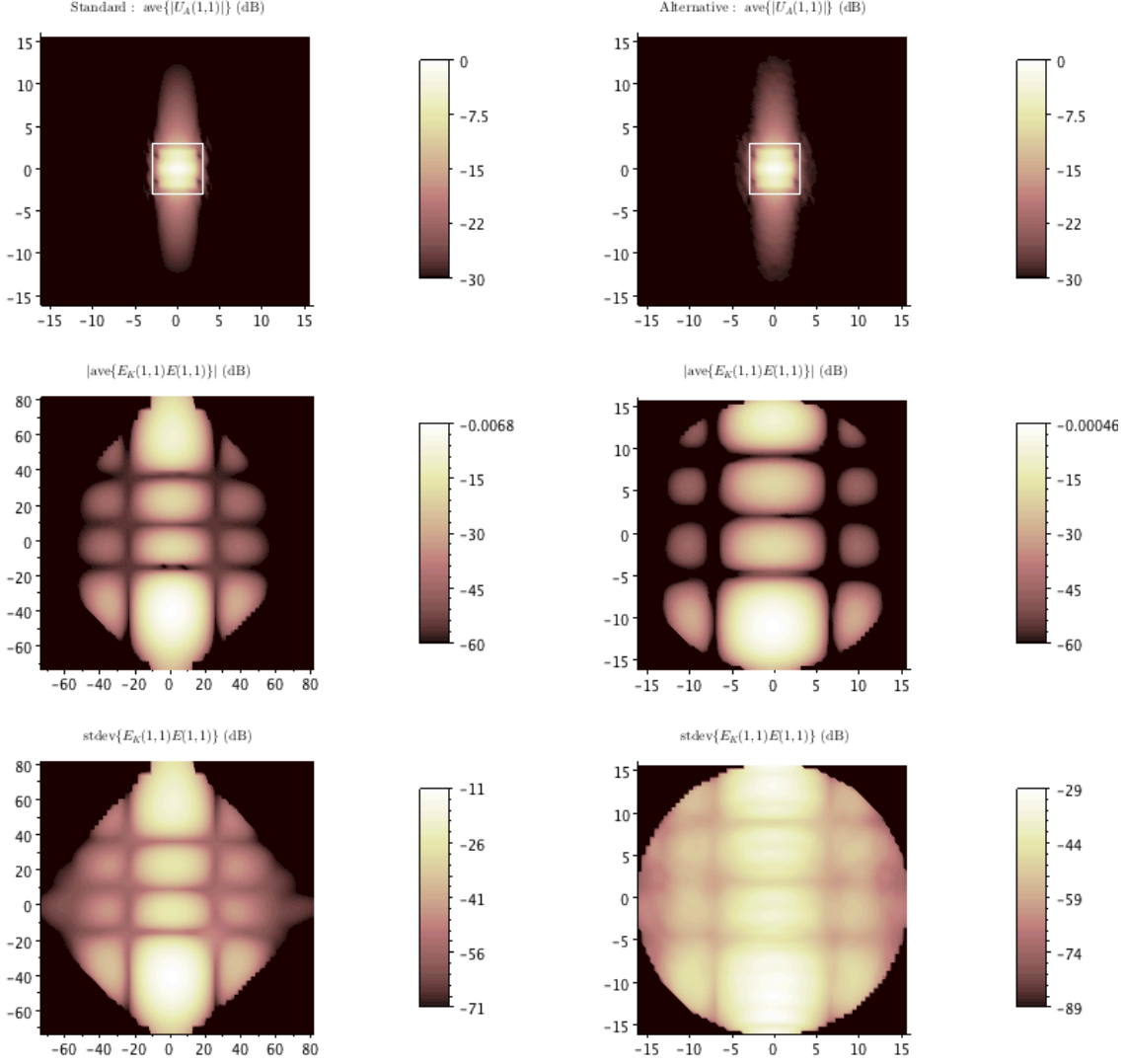


Figure 4: The panels show gridding kernels and the associated gridded angular response for the functions shown in figure 1. They demonstrate that the alternative kernels discussed in section 3 can have compact support, and the level to which they can suppress differences between the response of the gridded samples. The top left and top right panels show images of $|\mathcal{F}\{E_{k,11}^*(\boldsymbol{\sigma})\}|$ (see section 2) and $|\mathcal{F}\{\bar{E}_{11}^*(\boldsymbol{\sigma})\bar{E}_{11}(\boldsymbol{\sigma})/(E_{k,11}(\boldsymbol{\sigma}) + \epsilon)\}|$ (see section 3), respectively. For the latter, ϵ was set to 0.1% of the maximum value of $|E_{k,11}(\boldsymbol{\sigma})|$. The tile primary beams are modelled as the superposition of 16 dipole angular response matrices with various dipole-based errors, as described in the main text and shown in figure 1. The top right panel demonstrates a gridding kernel that divides out the angular response of a sample but retains compact support. Using the regions within the white boxes that are indicated in the top panels to generate gridding kernels, the resulting gridded angular weighting functions, $E_{K,k}(\boldsymbol{\sigma})E_k(\boldsymbol{\sigma})$, are shown down each column, where $E_{K,k}(\boldsymbol{\sigma})$ represents the FFT of the cropped region for sample k . The middle row shows the average gridded response, the bottom row shows the standard deviation. The sample-to-sample standard deviation after gridding with alternative kernels is almost 20 dB less than the standard deviation after gridding with standard kernels, which will lead to less variation in the PSF and smaller side-lobes (as will uniform or robust weighting).